

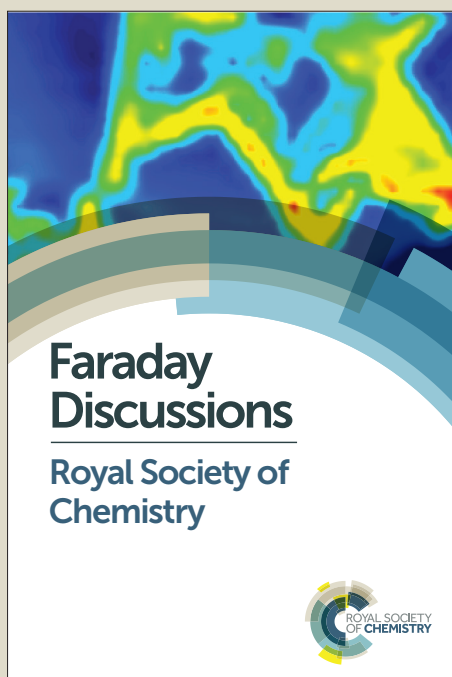
Faraday Discussions

Accepted Manuscript



This manuscript will be presented and discussed at a forthcoming Faraday Discussion meeting. All delegates can contribute to the discussion which will be included in the final volume.

Register now to attend! Full details of all upcoming meetings: <http://rsc.li/fd-upcoming-meetings>



This is an *Accepted Manuscript*, which has been through the Royal Society of Chemistry peer review process and has been accepted for publication.

Accepted Manuscripts are published online shortly after acceptance, before technical editing, formatting and proof reading. Using this free service, authors can make their results available to the community, in citable form, before we publish the edited article. We will replace this *Accepted Manuscript* with the edited and formatted *Advance Article* as soon as it is available.

You can find more information about *Accepted Manuscripts* in the [Information for Authors](#).

Please note that technical editing may introduce minor changes to the text and/or graphics, which may alter content. The journal's standard [Terms & Conditions](#) and the [Ethical guidelines](#) still apply. In no event shall the Royal Society of Chemistry be held responsible for any errors or omissions in this *Accepted Manuscript* or any consequences arising from the use of any information it contains.

This article can be cited before page numbers have been issued, to do this please use: S. Yang, H. Chen, Z. Wei, Y. Yi, K. Yan and J. Wang, *Faraday Discuss.*, 2014, DOI: 10.1039/C4FD00155A.

Liquid Phase Deposition of TiO₂ Nanolayer Affords CH₃NH₃PbI₃/Nanocarbon Solar Cells with High Open-Circuit Voltage

Haining Chen,^{a,†} Zhanhua Wei,^{a,†} Keyou Yan,^a Ya Yi,^b Jiannong Wang,^b and Shihe Yang^{a,*}

DOI: 10.1039/b000000x [DO NOT ALTER/DELETE THIS TEXT]

Hybrid organic/inorganic perovskite solar cell is attracting intense attention and further developments largely hinge on understanding the fundamental issues involved in the cell operation. In this paper, liquid phase deposition (LPD) method is developed to design and grow TiO₂ nanolayer at room temperature for carbon-based perovskite solar cells. The TiO₂ nanolayer grown on FTO glass is compact but polycrystalline consisting of tiny anatase TiO₂ nanocrystals intimately stacked together. Directly exploiting this TiO₂ nanolayer in a solar cell of TiO₂ nanolayer/CH₃NH₃PbI₃/nanocarbon, we have achieved a V_{oc} as high as 1.07 V, the highest value reported so far for hole transporter-free CH₃NH₃PbI₃ solar cells. This is rationalized by the slower electron injection and longer electron lifetime due to the TiO₂ nanolayer, which enhances the electron accumulation in CH₃NH₃PbI₃ and consequently the V_{oc} . By employing a rutile TiO₂ NR array as a base structure for the LPD-TiO₂ nanolayer to support the CH₃NH₃PbI₃ layer, the photocurrent density is considerably increased without obviously compromising V_{oc} (1.01 V). As a result, the power conversion efficiency is boosted from 3.67 % to 8.61 %. More elaborate engineering of the TiO₂ nanolayer by LPD in conjunction with a judicious interfacing with other components has the potential to achieve higher performance of this type of solar cells.

1 Introduction

The hybrid organic/inorganic perovskite solar cells are very promising to offer high conversion efficiency while permitting low-cost solution based manufacturing. In the last five years, the efficiencies of the perovskite solar cells have skyrocketed from the initial 3 % to 17.9 %¹⁻¹¹, and over 20 % efficiencies are expected to be achieved in the near future with the progress in basic understanding of their working mechanism and the further development of more controllable fabrication processes^{4, 12-14}. Furthermore, through integration with silicon panels to create tandem cells, obtaining much higher efficiencies may be possible. Therefore, perovskite solar cells are predicted as the “next big thing” in photovoltaics.

The hybrid organic/inorganic perovskite solar cells typically consist of TiO₂/perovskite/hole transport material (HTM)/noble metal electrode. However, other cell structures are exploited and developed due to the excellent photovoltaic properties of the perovskite materials (CH₃NH₃PbI₃ and CH₃NH₃PbI_{3-x}Cl_x), including strong solar absorption^{2, 3, 7}, ambipolar charge transport^{4, 13, 15}, long balanced carrier diffusion lengths (100-1000 nm)^{16, 17}. Among those new cell

structures, HTM-free perovskite solar cells have become more and more promising, which avoid using unstable and/or expensive organic HTM (mainly spiro-OMeTAD)¹⁸⁻²⁷. Very recently, carbon-based perovskite solar cells stand out for their high efficiencies (a certified efficiency of 12.8 %) and the obvious advantages of the carbon electrode, such as material abundance, low cost, superior stability and printable fabrication processes²⁴⁻²⁸.

Regardless of the development of different cell structures, TiO₂ nanolayer (dense layer and/or mesoporous layer) is still needed for high efficiency perovskite solar cells. In dye-sensitized solar cells (DSSCs), TiO₂ nanolayer accepts injected electrons and is the unique electron transport pathway. However, since perovskite itself is an efficient electron transporter, TiO₂ nanolayer is not a unique electron transport pathway in perovskite solar cells^{13, 15}. And it has been proposed that partial electron accumulation and transport in perovskite is favorable for obtaining higher open-circuit voltage (V_{oc}) (due to the higher conduction band edge of perovskite than that of TiO₂) and thus higher efficiency^{3, 29, 30}.

Herein, we report the growth of a TiO₂ nanolayer by the liquid phase deposition (LPD) method^{31, 32} at room temperature for CH₃NH₃PbI₃/nanocarbon solar cells. In contrast to the commonly used TiO₂ nanolayer, this unique LPD-TiO₂ nanolayer could slow electron injection and prolong electron lifetime, which as a result enhanced the electron accumulation in CH₃NH₃PbI₃ and led to a considerably higher V_{oc} of 1.07 V, the highest value for HTM-free CH₃NH₃PbI₃ solar cells. We have further used a TiO₂ nanorod (NR) array as a base structure for this LPD-TiO₂ nanolayer to support the CH₃NH₃PbI₃ photoactive layer, and achieved a significantly boosted photocurrent density without obviously compromising V_{oc} (1.01 V), promoting the cell efficiency from 3.67 % to 8.61 %.

2 Experimental

2.1 Preparation

Preparation of LPD-TiO₂ nanolayers. To prepare TiO₂ nanolayers by LPD method^{31, 32}, the reaction solutions were firstly prepared by dissolving 0.05 M (NH₄)₂TiF₆ and 0.15 M boric acid (H₃BO₃) in distilled water. Then, FTO glasses were placed in the reaction solution with the FTO thin film sides facing down. The reaction was carried out at room temperature and the thickness of the TiO₂ nanolayers was controlled by varying the reaction duration.

TiO₂ NR array as a base structure for LPD-TiO₂ nanolayers. The TiO₂ NRs were grown on FTO glass using the hydrothermal method. Briefly, FTO glass was immersed in the Teflon-lined stainless steel autoclave (100 mL capacity) containing 0.6 mL of titanium (IV) butoxide, 25 mL of deionized (DI) water and 25 mL of concentrated HCl (36-38 %) ^{8, 33}. And hydrothermal process was carried out by putting the autoclave into an oven and held at 180 °C for 3 h. The autoclave was then removed from the oven and cooled down to room temperature naturally. The samples were taken out and washed with DI water, and finally annealed at 500 °C for 1 h in air.

To deposit a LPD-TiO₂ nanolayer on the FTO glass/TiO₂ NR array, the TiO₂ NR array was immersed in the LPD solutions with the TiO₂ NR array side facing down.

Fabrication of CH₃NH₃PbI₃/nanocarbon solar cells. First, the TiO₂ nanolayers were pre-heated to 100 °C. Then, the N,N-dimethylformamide solution containing 460 mg/mL PbI₂, which was pre-heated to 100 °C, was spin coated on the TiO₂

nanolayer-coated FTO glasses at 2500 r.p.m. for 30 s⁶. After being dried in air, the samples were heated up to 100 °C and kept for 15 min to crystallize the PbI₂. Finally, the samples were cooled down naturally to room temperature again.

The deposition of nanocarbon electrode was carried out by spin coating a chlorobenzene suspension of 15 mg/mL nanocarbon particles on the top of TiO₂/PbI₂. Then, the samples were dried at room temperature and heated at 100 °C for 5 min.

Conversion of the PbI₂ layer to CH₃NH₃PbI₃ was performed by spin coating a 2-propanol solution containing 10 mg/mL CH₃NH₃I on the top of TiO₂/PbI₂/nanocarbon at 100 r.p.m. for 20 s⁶. Finally, the samples were gently dried under a flow of dry air and then heated up to 100 °C and kept for 15 min to get the CH₃NH₃PbI₃/nanocarbon solar cells.

For measurement, another piece of FTO glass, serving as assistant collecting electrode, was clamped with the above CH₃NH₃PbI₃/nanocarbon component for solar cell performance evaluation.

Preparation of USP-TiO₂ nanolayer. A commonly used TiO₂ dense layer for control experiments was deposited on FTO by a home-made ultrasonic spray deposition (USP) system at 500 °C using titanium diisopropoxide bis(acetylacetonate) solution (0.05 M, ethanol) as precursor and air as carrier gas.

2.2 Characterizations

Morphology was evaluated on a scanning electron microscopy (SEM, JEOL6700F) at an accelerating voltage of 5 kV. X-ray diffraction (XRD) patterns were recorded on a Philips PW-1830 X-ray diffractometer with Cu K α radiation (K = 0.15418 nm). Diffuse reflectance UV-vis absorption spectra were recorded on a Perkin-Elmer UV-vis spectrophotometer (model Lambda 20). The XPS spectra were measured on a Perkin-Elmer model PHI 5600 XPS system with a resolution of 0.3-0.5 eV from a monochromated aluminium anode X-ray source with MoK α radiation (1486.6 eV). Ultraviolet photoelectron spectroscopy (UPS) measurements were performed on a photoelectron spectrometer (Kratos Analytical, AXIS-ultra-DLD) with He (I) excitation of 21.22 eV and pass energy of 5 eV.

Mott-Schottky (M-S) plot was acquired using a CHI 660A electrochemical analyzer in a three-electrode system. The LPD-TiO₂ nanolayer, an Ag/AgCl electrode and a Pt wire served as the working, reference and counter electrodes, respectively. The electrolyte used for this measurement contained 1 M KOH and the frequency was set at 3 kHz.

2.3 Photovoltaic measurements

The solar light simulator (Newport solar simulator, model number 6255, 150 W Xe lamp, AM 1.5 global filter) was calibrated to 1 sun (100 mW/cm²) using a silicon reference solar cell equipped with a KG-5 filter. A black metal shading mask (0.09 cm²) was used to define the illumination area of the cells to be tested and tightly packaged to prevent light incident from the edges. Current density-voltage (*J-V*) characteristic curves and open circuit voltage decay (OCVD) curves were recorded on an IM6x electrochemical workstation (ZAHNER-Elektrik GmbH & Co., KG, Germany). Incident-photo-to-current conversion efficiency (IPCE) was recorded using IPCE kit developed by ZAHNER-Elektrik in AC mode with frequency of 1 Hz. For time-resolved photoluminescence (TRPL) measurements, a tunable Ti:sapphire femtosecond-pulsed laser was used as the excitation light source, with an

excitation wavelength of 400 nm and an incident light intensity of 1 W/cm². A Hamamatsu C5680-04 streak camera was used for the TRPL experiments. The TRPL measurements were performed in the vacuum.

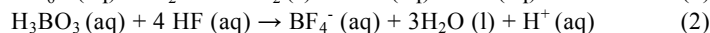
View Article Online

DOI: 10.1039/C4FD00155A

3. Results and discussion

3.1 The formation of the LPD-TiO₂ nanolayer and its influence on CH₃NH₃PbI₃/nanocarbon solar cells

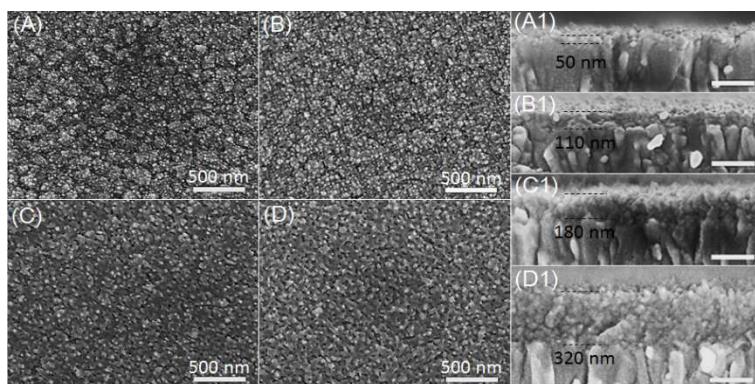
To prepare LPD-TiO₂ nanolayers, we used an aqueous solution containing 0.05 M (NH₄)₂TiF₆ and 0.15 M H₃BO₃. The LPD of metal oxide nanolayers was performed via a chemical equilibrium reaction between a metal fluoro-complex and a metal oxide in an aqueous solution^{31, 32}. Specifically, the deposition reactions of LPD-TiO₂ nanolayers can be expressed as:



Interestingly, H₃BO₃ here can serve as an F⁻ scavenger, which consumes the F⁻ ions (Eq. 2) and thus accelerates the hydrolysis reaction (Eq. 1). In this way, the LPD at low temperature^{31, 32} could produce partially crystalline TiO₂, which could be used to control the electron injection by modulating the TiO₂/perovskite interface.

SEM was firstly applied to evaluate the morphology of the LPD-TiO₂ nanolayers. As shown in Figure 1(A), although the surface feature of FTO glass could still be observed, the FTO substrate becomes rough in nanoscale due to the coverage of tiny nanoparticles after LPD for 6 h. The cross sectional SEM image in Figure 1(A1) shows that the film thickness is about 50 nm. As the LPD duration increases to 12 h, the surface feature of FTO glass could be hardly observed, demonstrating the formation of a relatively flat LPD-TiO₂ nanolayer. And the size of the tiny nanoparticles seems to be unchanged, suggesting that generating new crystal nucleus instead of the further growth of old crystals mainly promotes the growth of LPD-TiO₂ nanolayer, which is favorable for producing compact TiO₂ nanolayer. As indicated in Figure 1(B1), the LPD-TiO₂ nanolayer is very compactly covered on FTO glass with the thickness increasing to about 110 nm.

When the LPD duration was extended to 18 h, the size of the tiny nanoparticles is still very small (Figure 1(C)), but small pores with the size similar to that of tiny particles are homogeneously dispersed on the surface. As depicted in Figure 1(C1), the film thickness is increased to about 180 nm and the film is still intimately covered on the surface of FTO glass. Further extending the LPD duration to 36 h resulted in a slight increase in sizes of both the tiny nanoparticles and the pores (Figure 1(D)) with the film thickness increasing to about 320 nm (Figure 1(D1)). As indicated in the SEM images and observed during experiments, the LPD-TiO₂ nanolayers show excellent adherence to the FTO glass, which even could not be destroyed by ultrasonic agitation.



View Article Online
DOI: 10.1039/C4FD00155A

Figure 1 Morphology evaluation of LPD-TiO₂ nanolayer with different LPD durations. Top-view SEM images: (A) 6 h, (B) 12 h, (C) 18 h and (D) 36 h. (A1), (B1), (C1) and (D1) are the corresponding cross sectional SEM images. Scale bar: 200 nm.

XRD patterns and Raman spectra were recorded to evaluate the composition and structural phase of the LPD-TiO₂ nanolayers. As shown in Figure 2(A), in addition to the characteristic diffraction peaks of FTO glass, other peaks at 25.0° and 47.8° are observed, which can be well indexed to the (101) and (200) planes of anatase TiO₂, respectively. Similarly, as indicated in Figure 2(B), the peaks at 166 cm⁻¹, 501 cm⁻¹ and 623 cm⁻¹ can be assigned to the three Raman-active modes of *E_g*, *A_{1g}* and *E_g* of anatase TiO₂³⁴⁻³⁸, respectively. However, compared with the corresponding Raman shift data in the literature³⁴⁻³⁶, obvious blue shifts occurs, plausibly due to the much smaller size of the anatase TiO₂ crystals prepared by LPD³⁸. According to the relation between the position of *E_g* mode (ω) and the diameter of TiO₂ nanocrystals (L)³⁸,

$$\omega = 100(1/L^{1.5}) + \omega_0 \quad (3)$$

where $\omega_0 = 142$ cm⁻¹, the diameter of the anatase TiO₂ nanocrystals should be only about 3 nm. Together, both the XRD and Raman shift results demonstrate that the LPD-TiO₂ nanolayer is in anatase phase and composed of tiny nanocrystals. And both the peak intensities of XRD pattern and Raman shift are low, again suggesting the low crystallinity of the anatase TiO₂ nanolayers.

TEM was also applied to characterize the LPD-TiO₂ nanolayers. It can be readily seen in Figure 2(C) that the LPD-TiO₂ nanolayers are polycrystalline. As indicated by the white line circles, the nanocrystal diameter is about several nanometers, consistent with the Raman shift result. Note that these tiny nanocrystals are compactly stacked together, making it possible to form a uniform film. The observed electron diffraction pattern (Figure 2(D)) can be readily indexed to the (101), (004), (200), (211), (105) and (204) planes of anatase TiO₂, confirming the polycrystalline nature of anatase TiO₂ nanolayer prepared by LPD.

To study the semiconducting properties of the LPD-TiO₂ nanolayer, *Mott-Schottky* (*M-S*) plot was first measured. As shown in Figure 2(E), the *M-S* plot shows a positive slope, indicating an *n*-type semiconductor behavior. The free charge carrier density in LPD-TiO₂ nanolayer could be calculated using Eq. 4³⁹:

$$N_c = (2/e_0\epsilon\epsilon_0)[d(1/C^2)/dV]^{-1} \quad (4)$$

where e_0 is the electron charge, ϵ the dielectric constant of anatase TiO₂, ϵ_0 the permittivity of vacuum, N_c the carrier density and V the applied potential. N_c for the LPD-TiO₂ nanolayer is calculated to be about 1.27×10^{20} cm⁻³. This high N_c will be

favorable for electron transport in, for example, solar cells.

From the UV-vis absorption spectrum in Figure 2(F), the absorption threshold of the LPD-TiO₂ nanolayer is obtained at about 390 nm, corresponding to the electronic transition from the valence band (VB) to the conduction band (CB) of anatase TiO₂. The $(\alpha h\nu)^{1/2}$ - $h\nu$ plot in the inset of Figure 2(F) indicates that the band gap (E_g) values of LPD-TiO₂ nanolayer is about 3.12 eV, consistent with the typical value for anatase TiO₂. Ultraviolet photoelectron spectroscopy (UPS) result in Figure 2(G) indicates that the VB edge for the LPD-TiO₂ nanolayer is about -7.19 eV with reference to the vacuum level. The CB edge of the LPD-TiO₂ nanolayer is calculated to be about -4.07 eV using the relation: $E_g = E_{CB} - E_{VB}$, which is lower than the CB edge of CH₃NH₃PbI₃. Therefore, the energy band structure of the LPD-TiO₂ nanolayer is suitable for electron injection in the CH₃NH₃PbI₃/nanocarbon solar cells.

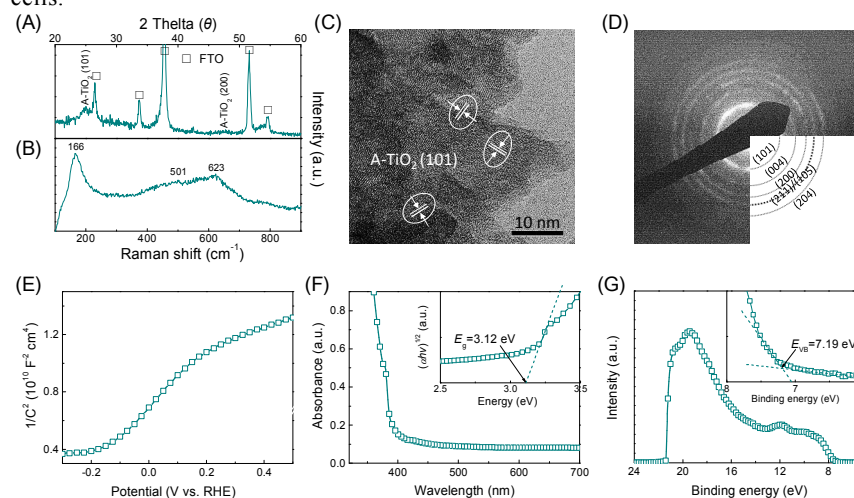


Figure 2 Composition and structural phase of the LPD-TiO₂ nanolayer: (A) XRD pattern, (B) Raman spectrum, (C) HRTEM images, and (D) electron diffraction pattern. Semiconducting properties of the LPD-TiO₂ nanolayer: (E) M - S plot, (F) UV-vis absorption spectrum, and (G) UPS spectrum. Inset in (F) is $(\alpha h\nu)^{1/2}$ - $h\nu$ plot and inset in (G) is the zoomed region between 6-8 eV of the UPS spectrum.

To fabricate the CH₃NH₃PbI₃/nanocarbon solar cells based on the LPD-TiO₂ nanolayer, the processes illustrated in Figure 3(A) are applied. Firstly, the N,N-dimethylformamide solution containing 460 mg/mL PbI₂ was spin coated on LPD-TiO₂ nanolayer⁶. After crystallization, a vivid PbI₂ layer composed of sheet-like nanocrystals is deposited on the LPD-TiO₂ nanolayer, with a thickness of about 300 nm (Figure S1(A)). Nanocarbon electrode was coated on the top of FTO/TiO₂/PbI₂ by spin coating a chlorobenzene solution containing 15 mg/mL nanocarbon particles. After drying, a porous nanocarbon layer about tens of micrometers is formed on the top of the PbI₂ layer with the nanocarbon nanoparticles of about 30-80 nm in diameter, as shown in Figure S1(B) and (C). Then, the 2-propanol solution containing 10 mg/mL CH₃NH₃I was spin coated on the top of FTO/TiO₂/PbI₂/nanocarbon⁶. Due to the porous structure of nanocarbon electrode, CH₃NH₃I solution could penetrate through the nanocarbon electrode to reach and react with the PbI₂ layer to generate CH₃NH₃PbI₃. As a result, PbI₂ layer would be

converted to $\text{CH}_3\text{NH}_3\text{PbI}_3$ and this conversion could be further promoted after heating at 100 °C for 15 min.

Figure 3(B) represents the cross-sectional SEM image of the typical $\text{TiO}_2/\text{CH}_3\text{NH}_3\text{PbI}_3/\text{nanocarbon}$ solar cells, showing a clear layer-by-layer structure. The cubic crystal could be vividly observed at the $\text{CH}_3\text{NH}_3\text{PbI}_3$ interlayer, implying the high quality of $\text{CH}_3\text{NH}_3\text{PbI}_3$ crystals prepared by our preparation strategy. As expected, the thickness of the $\text{CH}_3\text{NH}_3\text{PbI}_3$ interlayer is increased to about 400 nm in comparison with that of PbI_2 layer because the volume would be increased after the conversion of PbI_2 to $\text{CH}_3\text{NH}_3\text{PbI}_3$. As a result, through a careful observation, a fraction of the bottom nanocarbon layer attaching on the PbI_2 layer is imbedded in $\text{CH}_3\text{NH}_3\text{PbI}_3$ layer, forming a very intimate contact between $\text{CH}_3\text{NH}_3\text{PbI}_3$ and nanocarbon layers favorable for hole extraction in operating solar cells.

The energy level diagram and charge transfer processes in the $\text{CH}_3\text{NH}_3\text{PbI}_3/\text{nanocarbon}$ solar cells are illustrated in Figure 3(C). When $\text{CH}_3\text{NH}_3\text{PbI}_3$ is excited by light illumination, electrons and holes are generated on the CB and VB, respectively. Since the CB of the LPD- TiO_2 nanolayer is located at about -4.07 eV, electron injection will take place at the $\text{TiO}_2/\text{CH}_3\text{NH}_3\text{PbI}_3$ interface from the CB (-3.90 eV) of $\text{CH}_3\text{NH}_3\text{PbI}_3$ to the CB of TiO_2 , and these electrons will be finally collected at the FTO glass. In parallel, the holes are extracted by the nanocarbon electrode through the $\text{CH}_3\text{NH}_3\text{PbI}_3/\text{nanocarbon}$ interface from the VB (-5.40 eV) of $\text{CH}_3\text{NH}_3\text{PbI}_3$ to nanocarbon electrode (Fermi level: -5.0 eV).

Figure 3(D) exhibits the $J-V$ curves of the $\text{CH}_3\text{NH}_3\text{PbI}_3/\text{nanocarbon}$ solar cells based on the LPD- TiO_2 nanolayers with different thicknesses, and Table 1 lists the corresponding photovoltaic parameters. For comparison, the solar cells based on bare FTO glass was also prepared, and their performance was so poor and unstable that their $J-V$ curve could not be obtained. Comparatively, the LPD- TiO_2 nanolayer about 50 nm thick allowed us to obtain reproducible $J-V$ curves, but the V_{oc} is only about 0.18 V and the J_{sc} is also very low, resulting in a low η at about 0.18 %. As the film thickness is increased to 110 nm, the cell performance is obviously improved with a V_{oc} of 0.98 V and a J_{sc} of 3.44 mA/cm^2 , amounting to a η of 1.67 %.

Further thickening of the film to 180 nm continued to improve the cell performance with a V_{oc} as high as 1.07 V, which is the highest reported V_{oc} for HTM-free $\text{CH}_3\text{NH}_3\text{PbI}_3$ solar cells including carbon and Au-based $\text{CH}_3\text{NH}_3\text{PbI}_3$ solar cells. Since the CB of LPD- TiO_2 nanolayer is located at -4.07 eV, the maximum obtainable V_{oc} is about 0.93 V if the highest electron and lowest hole energy levels are assumed to be the CB of LPD- TiO_2 nanolayer and the Fermi level of nanocarbon (-5.0 eV), respectively. The ultrahigh V_{oc} (1.07 V) we obtained further verifies the proposition of carrier accumulation in $\text{CH}_3\text{NH}_3\text{PbI}_3$. What is more, also increased are J_{sc} and FF to 4.54 mA/cm^2 and 0.54, respectively, leading to a η of 2.62 %. Finally, when the film thickness is increased to 320 nm, V_{oc} is slightly decreased to 1.00 V, but J_{sc} continued to increase to 6.28 mA/cm^2 , corresponding to a η up to 3.67 %. It seems that the level of electron injection from perovskite to TiO_2 plays an important role in dictating the V_{oc} and J_{sc} .

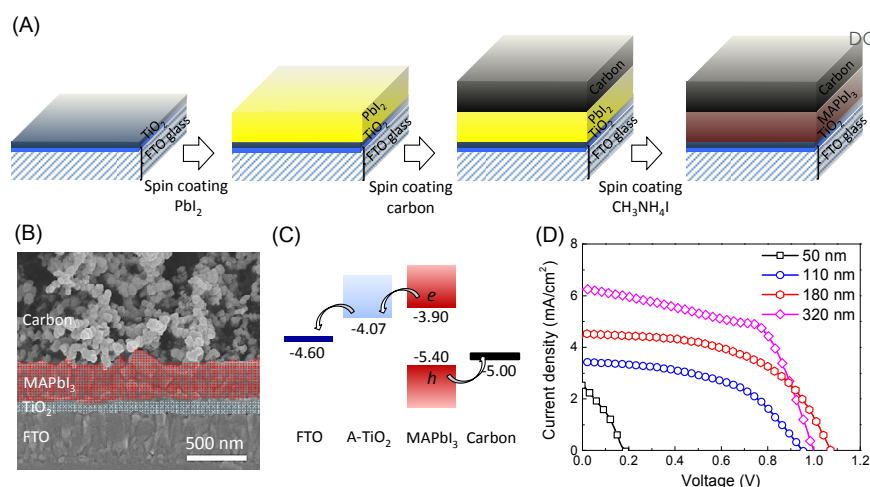


Figure 3 (A) Schematic illustration of the preparation processes of the $\text{CH}_3\text{NH}_3\text{PbI}_3/\text{nanocarbon}$ solar cells based on LPD- TiO_2 nanolayer. (B) Cross sectional SEM images and (C) Energy level diagram and charge transfer processes of the $\text{CH}_3\text{NH}_3\text{PbI}_3/\text{nanocarbon}$ solar cells. And (D) $J-V$ curves of the $\text{CH}_3\text{NH}_3\text{PbI}_3/\text{nanocarbon}$ solar cells based on the LPD- TiO_2 nanolayers with different thicknesses.

Table 1 Photovoltaic parameters obtained from the $\text{CH}_3\text{NH}_3\text{PbI}_3/\text{nanocarbon}$ solar cells based on the LPD- TiO_2 nanolayers with different LPD durations (or film thicknesses) on FTO glass and FTO glass/ TiO_2 NRs.

Substrate	LPD duration (film thickness)	V_{oc} (V)	J_{sc} (mA/cm ²)	FF	η (%)
FTO glass	6 h (50 nm)	0.18	2.50	0.40	0.18
	12 h (110 nm)	0.95	3.44	0.51	1.67
	18 h (180 nm)	1.07	4.54	0.54	2.62
	36 h (320 nm)	1.00	6.28	0.58	3.67
FTO glass/ TiO_2 NRs	0 h	0.54	9.35	0.27	1.36
	2 h	0.67	12.98	0.35	3.04
	5 h	1.01	14.20	0.60	8.61
	9 h	0.89	15.74	0.49	6.86

3.2 Insight into the influence of the LPD- TiO_2 nanolayer on the cell performance

To gain a deeper insight into the performance enhancement mechanism of the LPD- TiO_2 nanolayer, a commonly used dense anatase TiO_2 nanolayer with high crystallinity (Figure S2) for perovskite solar cells was prepared by ultrasonic spray pyrolysis (USP). For meaningful comparison, the thicknesses of the two TiO_2 nanolayers were controlled at about 100 nm. As shown in Figure 4(A), the current densities for both solar cells are not very high since they are compact and thin. But it can still be seen that the USP- TiO_2 nanolayer based solar cells achieve a higher J_{sc} (5.12 mA/cm²) than that the LPD- TiO_2 nanolayer based ones (3.02 mA/cm²), whereas the latter achieves a considerably higher V_{oc} (0.94 V) and FF (0.56) than the former (V_{oc} =0.78 V and FF=0.31). As a result, the former achieves a η of 1.63 %, which is higher than the latter one (1.37 %).

To pin down the origin of the performance difference between these two TiO_2 nanolayers, TRPL was first performed to investigate the electron injection rate from

CH₃NH₃PbI₃ to TiO₂ nanolayers. Figure 4(B) presents the streak camera images of TRPL, which map the PL decays at different wavelengths and provide an overview of the transient spectral behaviors. As can be easily observed, bare CH₃NH₃PbI₃ exhibits the slowest PL decays, while accelerated PL decays occurs to the two TiO₂ nanolayers due presumably to the electron injection. More interestingly, the PL decay is slower for CH₃NH₃PbI₃ on the LPD-TiO₂ nanolayer than that on the USP-TiO₂ nanolayer, suggesting the slower electron injection for the former.

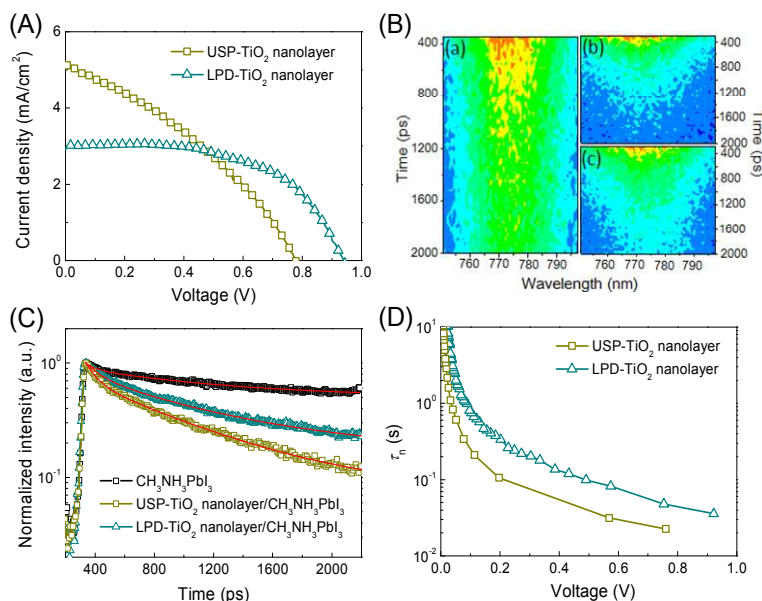
The PL decay curves extracted from Figure 4(B) are displayed in Figure 4(C). The PL lifetime (τ), which is defined as the time when the PL intensity decreases to 1/e of the original value, is calculated for the CH₃NH₃PbI₃ on the LPD-TiO₂ nanolayer to be about 880 ps, which is lower than that on the USP-TiO₂ nanolayer, about 515 ps. The slower electron injection could partially account for the lower J_{sc} for the LPD-TiO₂ nanolayer. But more importantly, this slower electron injection is expected to accumulate electrons in CH₃NH₃PbI₃, causing an increase in V_{oc} if recombination loss in the solar cells is not significant.

Further information on the recombination loss in the solar cells can be obtained from the electron lifetime (τ_n) measured by the OCVD technique. OCVD curves were recorded immediately after the interruption of light illumination and τ_n was determined according to Eq. 5⁴⁰.

$$\tau_n = k_B T / q \cdot (dV_{oc}/dt)^{-1} \quad (5)$$

where k_B is the Boltzmann constant, T the absolute temperature and q the positive elementary charge. As shown in Figure 4(D), the τ_n for the CH₃NH₃PbI₃/nanocarbon solar cells based on the LPD-TiO₂ nanolayer is about 2-4 times longer than that based on the USP-TiO₂ nanolayer in the whole potential range, implying a slower recombination reaction in the former solar cells than in the latter in keeping with the higher V_{oc} and FF.

Conclusively, the slower electron injection and longer electron lifetime in the LPD-TiO₂ nanolayer based solar cells are held responsible for their increased V_{oc} and FF compared with those in USP-TiO₂ nanolayer based solar cells. The lower crystallinity and/or the smaller size of TiO₂ nanocrystals in LPD-TiO₂ nanolayer may account for the slower electron injection, while the slower electron recombination hints at a better interface contact between the LPD-TiO₂ nanolayer and CH₃NH₃PbI₃. Clearly, further investigations are needed to better understand the detailed causality involved. Nevertheless, it has been clearly demonstrated that the LPD-TiO₂ nanolayer holds promise for designing perovskite solar cells with high V_{oc} and FF.



View Article Online
DOI: 10.1039/C4FD00155A

Figure 4 Performance comparison between the USP-TiO₂ nanolayer and LPD-TiO₂ nanolayer. (A) *J*-*V* curves of CH₃NH₃PbI₃/nanocarbon solar cells; (B) TRPL streak camera images of (a) CH₃NH₃PbI₃, (b) USP-TiO₂ nanolayer/CH₃NH₃PbI₃ and (c) LPD-TiO₂ nanolayer/CH₃NH₃PbI₃, and (C) Fitted TRPL with biexponential decay traces; and (D) τ_n -*V*_{oc} curves of of CH₃NH₃PbI₃/nanocarbon solar cells.

Though the ultrahigh *V*_{oc} was achieved for the CH₃NH₃PbI₃/nanocarbon solar cells based on the LPD-TiO₂ nanolayers, the photocurrent densities were low, which limited the power conversion efficiencies. The low current density should be attributed to the fact that all these LPD-TiO₂ nanolayers are flat and compact, which makes it difficult to achieve a homogenous coverage of a sufficiently thick and effective CH₃NH₃PbI₃ layer through solution-based processes^{15, 41, 42}. This low quality CH₃NH₃PbI₃ layer would lead to a poor light absorption of CH₃NH₃PbI₃/nanocarbon solar cells. To resolve this problem, we made an attempt to employ TiO₂ NR array grown on FTO glass as a base structure for the LPD-TiO₂ nanolayers to support a high quality CH₃NH₃PbI₃ layer as described below.

3.3 LPD-TiO₂ nanolayers on a rutile NR array for the CH₃NH₃PbI₃/nanocarbon solar cells

To grow TiO₂ NR array, a typical hydrothermal method was applied with FTO thin film as seed layer. After 3 h of hydrothermal treatment, TiO₂ NRs with an average length of 600 nm were grown on FTO glass, as shown in Figure 5(A). The diameter of TiO₂ NRs ranges from 40 to 80 nm. After LPD for 2 h, the surface of the TiO₂ NRs becomes rough (Figure 5(B)) in comparison with those in Figure 5(A), well indicating the secondary growth of TiO₂ on the TiO₂ NRs. Besides, the exposed surface of FTO glass between TiO₂ NRs is also covered with a new growth layer. As the LPD duration was extended to 5 h, the surface of TiO₂ NRs becomes more rough, resulting in an obvious increase in diameter (Figure 5(C)), and the overlayer on the exposed surface of FTO glass between TiO₂ NRs is also thickened. On further increasing the LPD duration to 9 h, an obvious nanobranched structure appears to be

formed, and the space between TiO₂ NRs is reduced accompanied by the crowded roots of the TiO₂ NRs (Figure 5(D)).

Next XRD patterns and Raman spectra were acquired to evaluate the composition of the samples before and after LPD. For bare TiO₂ NRs, in addition to the characteristic diffraction peaks of FTO glass (Figure 5(E)), the diffraction peaks at 27.3°, 36.0°, 41.2°, 51.6°, 54.4° and 62.7° are indexed to (110), (101), (111), (211), (220) and (002) planes of rutile TiO₂, respectively. After LPD, two new diffraction peaks at 25.0° and 47.9° that could be indexed to the (101) and (200) planes of anatase TiO₂, respectively, are observed, implying that anatase TiO₂ was deposited on the rutile TiO₂ NRs after LPD.

The Raman spectra in Figure 5(F) indicate that only the peaks at 238 cm⁻¹, 445 cm⁻¹ and 608 cm⁻¹ are observed for bare TiO₂ NRs, consistent with the three Raman-active modes of B_{1g}, E_g and A_{1g} of rutile TiO₂^{43, 44}, respectively, confirming the rutile phase of TiO₂ NRs. After LPD, a new and obvious peak accompanying with those of rutile TiO₂ is detected at 166 cm⁻¹, which can be easily assigned to the E_g mode of anatase TiO₂. Therefore, both XRD and Raman shift results corroborate that the secondary growth through LPD forms the anatase TiO₂-coated layer on the rutile TiO₂ NR array.

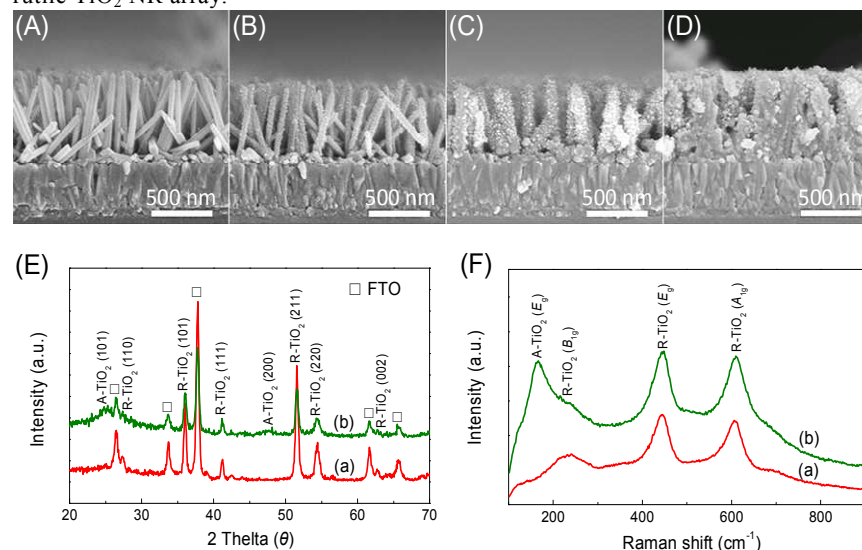


Figure 5 Cross-sectional SEM images of the TiO₂ NRs/LPD-TiO₂ nanolayers with different LPD durations: (A) 0 h, (B) 2 h, (C) 5 h and (D) 9 h. Phase structure and composition characterizations of (a) pristine TiO₂ NRs and (b) TiO₂ NRs/LPD-TiO₂ nanolayer: (A) XRD patterns and (B) Raman shifts.

To tap into the structural features of the TiO₂ NRs/LPD-TiO₂ nanolayer, the TEM technique was further applied. For the bare TiO₂ NRs, the surface is smooth as shown in Figure 6(A). HRTEM in Figure 6(A1) demonstrates the single-crystalline structure of the TiO₂ NRs with the growth orientation along with [001] direction. After LPD for 2 h, a new outer layer with a thickness of about several nanometers is deposited, which courses the surface of TiO₂ NRs. HRTEM image in Figure 6(B1) demonstrates that the outlined fringes are consistent with the (101) planes of anatase TiO₂, further confirming the deposition of anatase TiO₂ polycrystalline nanolayer on

the surface of rutile TiO_2 NRs. The TEM image in Figure 6(C) indicates that the outer anatase TiO_2 nanolayer is thickened up to 30-40 nm as the LPD duration extends to 5 h. Electron diffraction pattern in the inset of Figure 6(C) indicates that in addition to the diffraction spots of single rutile TiO_2 , the polycrystalline diffraction rings corresponding to the (101), (004) and (200) planes of anatase TiO_2 are also detected. Therefore, anatase TiO_2 polycrystalline nanolayer is deposited on the single rutile TiO_2 NRs after LPD. HRTEM image in Figure 6(C1) indicates that the size of the anatase TiO_2 nanocrystals is about several nanometers and they stack compactly on each other.

On the basis of the SEM, XRD, Raman shift and TEM results, it can be concluded that the nature of the TiO_2 nanolayer prepared by LPD is barely changed when the substrate is changed from FTO glass to FTO glass/ TiO_2 NRs, suggesting that the LPD method can be applied to deposit TiO_2 nanolayers on various substrates with similar material properties. To sum up, the structure and composition of the FTO glass/ TiO_2 NRs before and after LPD can be illustrated in Figure 6(D).

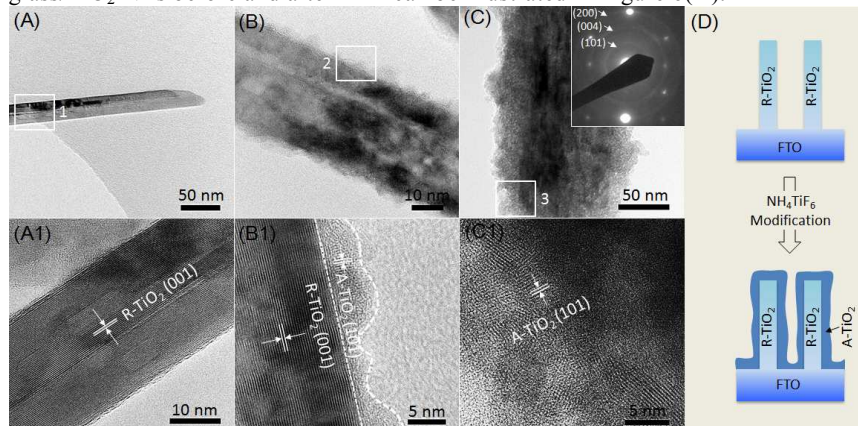


Figure 6 TEM images of TiO_2 NRs/LPD- TiO_2 nanolayers with different LPD durations: (A) 0 h, (B) 2 h and (C) 5 h. (A1), (B1) and (C1) represent the corresponding HRTEM images. (D) Schematic illustrating the structure and composition of the TiO_2 NRs before and after LPD.

To fabricate $\text{CH}_3\text{NH}_3\text{PbI}_3$ /nanocarbon solar cells based on the TiO_2 NRs/LPD- TiO_2 nanolayers, the same fabrication processes to those based on LPD- TiO_2 nanolayers were applied. The cross sectional SEM image of the solar cells in Figure 7(A) exhibits the vivid three-layer structure. The interlayer becomes compact in comparison with the cross sectional morphology of the TiO_2 NRs/LPD- TiO_2 nanolayers in Figure 5 due to the penetration and deposition of $\text{CH}_3\text{NH}_3\text{PbI}_3$ between TiO_2 NRs. The thickness of the interlayer is increased to 800 nm in comparison with that of the bare TiO_2 NRs/LPD- TiO_2 nanolayer (Figure 5), suggesting the deposition of a top layer of $\text{CH}_3\text{NH}_3\text{PbI}_3$ on the TiO_2 NRs. The scheme in Figure 7(B) clearly illustrates the cross sectional structure of the $\text{CH}_3\text{NH}_3\text{PbI}_3$ /nanocarbon solar cells based on the TiO_2 NRs/LPD- TiO_2 nanolayers.

The energy level diagram and charge transfer processes in the $\text{CH}_3\text{NH}_3\text{PbI}_3$ /nanocarbon solar cells based on TiO_2 NRs/LPD- TiO_2 nanolayers are illustrated in Figure 7(C). Photogenerated electrons on the CB of $\text{CH}_3\text{NH}_3\text{PbI}_3$ will firstly be injected into the CB of anatase TiO_2 (-4.07 eV) and then transferred to the

CB of rutile TiO_2 NRs (-4.10 eV) (see Figure S4). Finally, the electrons, after being transported through the single-crystalline rutile TiO_2 NRs, will be collected at the FTO glass. Meanwhile, the holes in the CB of $\text{CH}_3\text{NH}_3\text{PbI}_3$ will be extracted by the nanocarbon electrode.

Figure 7(D) presents the J - V curves of the $\text{CH}_3\text{NH}_3\text{PbI}_3$ /nanocarbon solar cells based on the TiO_2 NRs/LPD- TiO_2 nanolayers with different LPD durations. And Table 1 lists the corresponding photovoltaic parameters. The solar cells based on bare TiO_2 NRs exhibits a considerably higher $J_{\text{sc}}=9.35 \text{ mA/cm}^2$ than those based on LPD- TiO_2 nanolayers, which should be due to the deposition of the thicker effective $\text{CH}_3\text{NH}_3\text{PbI}_3$ photoactive layer. However, both V_{oc} and FF are low, 0.54 V and 0.27, respectively, implying the serious recombination at the exposed FTO glass/nanocarbon and/or the rutile TiO_2 /nanocarbon interfaces. As a result, only a low η (1.36 %) is obtained.

The LPD- TiO_2 nanolayer on the exposed FTO glass and the TiO_2 NR array appear to effectively suppress charge recombination at the above mentioned interfaces. In addition, electron accumulation in $\text{CH}_3\text{NH}_3\text{PbI}_3$ will also be enhanced. As a result, The V_{oc} , J_{sc} , FF and η are all obviously improved after the deposition of the LPD- TiO_2 nanolayer. And at the optimized LPD duration of 5 h, η as high as 8.61 % was obtained accompanied by high J_{sc} , V_{oc} and FF of 14.20 mA/cm^2 , 1.01 V and 0.60, respectively.

Therefore, by using the rutile TiO_2 NR array as a base structure for the LPD- TiO_2 nanolayer well to support a relative thick effective $\text{CH}_3\text{NH}_3\text{PbI}_3$ photoactive layer, we are able to achieve a considerably increased J_{sc} without obviously compromising V_{oc} (1.01 V) and hence a significantly boosted η .

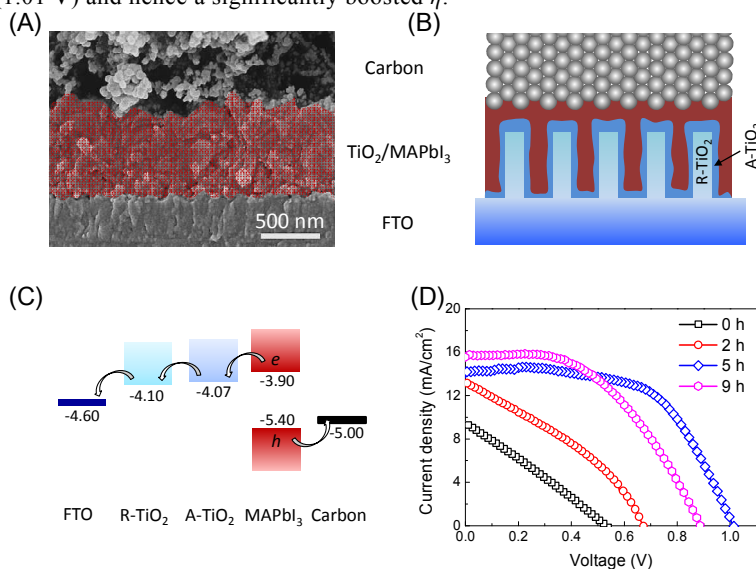


Figure 7 (A) Cross sectional SEM image, (B) cross sectional structure scheme, and (C) energy level diagram of the $\text{CH}_3\text{NH}_3\text{PbI}_3$ /nanocarbon solar cells based on the TiO_2 NRs/LPD- TiO_2 nanolayers. (D) J - V curves of the $\text{CH}_3\text{NH}_3\text{PbI}_3$ /nanocarbon solar cells based on the TiO_2 NRs/LPD- TiO_2 nanolayers with different LPD durations.

4. Conclusion

To control electron injection in carbon-based $\text{CH}_3\text{NH}_3\text{PbI}_3$ solar cells, we have prepared a TiO_2 nanolayer by the LPD method at room temperature. The TiO_2 nanolayer is compact and composed of tiny anatase TiO_2 nanocrystals intimately stacked together. Directly applying the TiO_2 nanolayer on FTO glass to $\text{CH}_3\text{NH}_3\text{PbI}_3$ /nanocarbon solar cells produced a V_{oc} as high as 1.07 V, which constitutes the highest value for HTM-free $\text{CH}_3\text{NH}_3\text{PbI}_3$ solar cells. Comparatively, the commonly used TiO_2 nanolayer could only achieve a low V_{oc} of 0.78 V. We have shown that the considerably higher V_{oc} for the solar cells based on the LPD- TiO_2 nanolayer is due to a slower electron injection and longer electron lifetime, which enhanced the electron accumulation in $\text{CH}_3\text{NH}_3\text{PbI}_3$. The application of the LPD- TiO_2 nanolayer to a rutile TiO_2 NR array was found to significantly enhance the photocurrent density of the corresponding solar cells without obviously compromising V_{oc} (1.01 V), upgrading the η from 3.67 % to 8.61 %. Higher performance is anticipated for the perovskite solar cells when the LPD- TiO_2 nanolayer is better interfaced with the other components of the devices.

ACKNOWLEDGMENT

This work was supported by the HK-RGC General Research Funds (GRF No. HKUST 606511, 605710 and 604410).

References

- ²⁰ ^a Department of Chemistry, William Mong Institute of Nano Science and Technology, The Hong Kong University of Science and Technology, Clear Water Bay, Kowloon, Hong Kong, China. chsyang@ust.hk.
- ^b Department of Physics, The Hong Kong University of Science and Technology, Clear Water Bay, Kowloon, Hong Kong, China.
- ²⁵ [†] These authors contributed equally to this work.
* Corresponding email: chsyang@ust.hk.
- [†] Electronic Supplementary Information (ESI) available: [supplementary SEM images, Raman shift, $(ah\nu)^2$ - $h\nu$ plot and UPS spectrum.]. See DOI: 10.1039/b000000x/.
- ³⁰ 1. A. Kojima, K. Teshima, Y. Shirai and T. Miyasaka, *J. Am. Chem. Soc.* 2009, **131**, 6050.
2. H. S. Kim, C. R. Lee, J. H. Im, K. B. Lee, T. Moehl, A. Marchioro, S. J. Moon, R. Humphry-Baker, J. H. Yum, J. E. Moser, M. Gratzel and N. G. Park, *Sci. Rep.* 2012, **2**, 591.
3. M. M. Lee, J. Teuscher, T. Miyasaka, T. N. Murakami and H. J. Snaith, *Science*, 2012, **338**, 643.
- ³⁵ 4. M. A. Green, A. Ho-Baillie and H. J. Snaith, *Nat. Photon.* 2014, **8**, 506.
5. H.-S. Kim, S. H. Im and N.-G. Park, *J. Phys. Chem. C*, 2014, **118**, 5615.
6. J. Burschka, N. Pellet, S. J. Moon, R. Humphry-Baker, P. Gao, M. K. Nazeeruddin and M. Gratzel, *Nature*, 2013, **499**, 316.
7. J. H. Im, C. R. Lee, J. W. Lee, S. W. Park and N. G. Park, *Nanoscale*, 2011, **3**, 4088.
- ⁴⁰ 8. J. Qiu, Y. Qiu, K. Yan, M. Zhong, C. Mu, H. Yan and S. Yang, *Nanoscale*, 2013, **5**, 3245.
9. Z. L. Zhu, J. A. Ma, Z. L. Wang, C. Mu, Z. T. Fan, L. L. Du, Y. Bai, L. Z. Fan, H. Yan, D. L. Phillips and S. H. Yang, *J. Am. Chem. Soc.* 2014, **136**, 3760.
10. M. Liu, M. B. Johnston and H. J. Snaith, *Nature*, 2013, **501**, 395.
- ⁴⁵ 11. N. J. Jeon, J. H. Noh, Y. C. Kim, W. S. Yang, S. Ryu and S. I. Seok, *Nat. Mater.* 2014, doi:10.1038/nmat4014.
12. N.-G. Park, *J. Phys. Chem. Lett.* 2013, **4**, 2423.
13. H. J. Snaith, *J. Phys. Chem. Lett.* 2013, **4**, 3623.
14. S. Kazim, M. K. Nazeeruddin, M. Gratzel and S. Ahmad, *Angew. Chem.* 2014, **53**, 2812.
15. T. C. Sum and N. Mathews, *Energy Environ. Sci.* 2014, **7**, 2518.
- ⁵⁰ 16. S. D. Stranks, G. E. Eperon, G. Grancini, C. Menelaou, M. J. Alcocer, T. Leijtens, L. M. Herz, A. Petrozza and H. J. Snaith, *Science*, 2013, **342**, 341.

17. G. Xing, N. Mathews, S. Sun, S. S. Lim, Y. M. Lam, M. Gratzel, S. Mhaisalkar and T. C. Sum, *Science*, 2013, **342**, 344.
18. L. Etgar, P. Gao, Z. S. Xue, Q. Peng, A. K. Chandiran, B. Liu, M. K. Nazeeruddin and M. Gratzel, *J. Am. Chem. Soc.* 2012, **134**, 17396.
19. W. Abu Laban and L. Etgar, *Energy Environ. Sci.* 2013, **6**, 3249.
20. S. Aharon, B. E. Cohen and L. Etgar, *J. Phys. Chem. C*, 2014, 140501072922009.
21. S. Aharon, S. Gamliel, B. El Cohen and L. Etgar, *Phys. Chem. Chem. Phys.* 2014, **16**, 10512.
22. J. Shi, J. Dong, S. Lv, Y. Xu, L. Zhu, J. Xiao, X. Xu, H. Wu, D. Li, Y. Luo and Q. Meng, *Appl. Phys. Lett.* 2014, **104**, 063901.
23. J. Shi, Y. Luo, H. Wei, J. Luo, J. Dong, S. Lv, J. Xiao, Y. Xu, L. Zhu, X. Xu, H. Wu, D. Li and Q. Meng, *ACS Appl. Mater. Interf.* 2014, **6**, 9711.
24. Z. Ku, Y. Rong, M. Xu, T. Liu and H. Han, *Sci. Rep.* 2013, **3**, 3132.
25. Z. Li, S. A. Kulkarni, P. P. Boix, E. Shi, A. Cao, K. Fu, S. K. Batabyal, J. Zhang, Q. Xiong, L. H. Wong, N. Mathews and S. G. Mhaisalkar, *Acs Nano*, 2014, **8**, 6797.
26. Y. Rong, Z. Ku, A. Mei, T. Liu, M. Xu, S. Ko, X. Li and H. Han, *J. Phys. Chem. Lett.* 2014, **5**, 2160.
27. Z. Wei, K. Yan, H. Chen, Y. Yi, T. Zhang, X. long, J. Li, L. Zhang, J. Wang and S. Yang, *Energy Environ. Sci.*, 2014, DOI: 10.1039/C4EE01983K.
28. A. Mei, X. Li, L. Liu, Z. Ku, T. Liu, Y. Rong, M. Xu, M. Hu, J. Chen, Y. Yang, M. Grätzel and H. Han, *Science*, 2014, **345**, 295.
29. D. Bi, S.-J. Moon, L. Häggman, G. Boschloo, L. Yang, E. M. Johansson, M. K. Nazeeruddin, M. Grätzel and A. Hagfeldt, *Rsc Adv.* 2013, **3**, 18762.
30. H.-S. Kim, I. Mora-Sero, V. Gonzalez-Pedro, F. Fabregat-Santiago, E. J. Juarez-Perez, N.-G. Park and J. Bisquert, *Nat. Commun.* 2013, **4**, 2242.
31. S. Deki, Y. Aoi, O. Hiroi and A. Kajinami, *Chem. Lett.* 1996, 433.
32. S. Deki, N. Yoshida, Y. Hiroe, K. Akamatsu, M. Mizuhata and A. Kajinami, *Solid State Ionics*, 2002, **151**, 1.
33. H. Chen, Z. Wei, K. Yan, Y. Bai, and S. Yang, *J. Phys. Chem. Lett.* 2014, **5**, 2890.
34. T. Ohsaka, *J. Phys. Soc. Jpn.* 1980, **48**, 1661.
35. W. F. Zhang, Y. L. He, M. S. Zhang, Z. Yin and Q. Chen, *J. Phys. D: Appl. Phys.* 2000, **33**, 912.
36. T. Ohsaka, F. Izumi and Y. Fujiki, *J. Raman Spectrosc.* 1978, **7**, 321.
37. J. C. Parker and R. W. Siegel, *J. Mater. Res.* 1990, **5**, 1246.
38. A. S. Pottier, S. Cassaignon, C. Chaneac, F. Villain, E. Tronc and J. P. Jolivet, *J. Mater. Chem.* 2003, **13**, 877.
39. M. G. Walter, E. L. Warren, J. R. McKone, S. W. Boettcher, Q. X. Mi, E. A. Santori and N. S. Lewis, *Chem. Rev.* 2010, **110**, 6446.
40. A. Zaban, M. Greenshtein and J. Bisquert, *ChemPhysChem*, 2003, **4**, 859.
41. G. E. Eperon, V. M. Burlakov, P. Docampo, A. Goriely and H. J. Snaith, *Adv. Funct. Mater.* 2014, **24**, 151.
42. A. Dualeh, N. Tétreault, T. Moehl, P. Gao, M. K. Nazeeruddin and M. Grätzel, *Adv. Funct. Mater.* 2014, **24**, 3250.
43. J. H. Nicola, C. A. Brunharoto, M. Abramovich and C. E. T. Concalvesdasila, *J. Raman Spectrosc.* 1979, **8**, 32.
44. G. Liu, Z. G. Chen, C. L. Dong, Y. N. Zhao, F. Li, G. Q. Lu and H. M. Cheng, *J. Phys. Chem. B*, 2006, **110**, 20823.